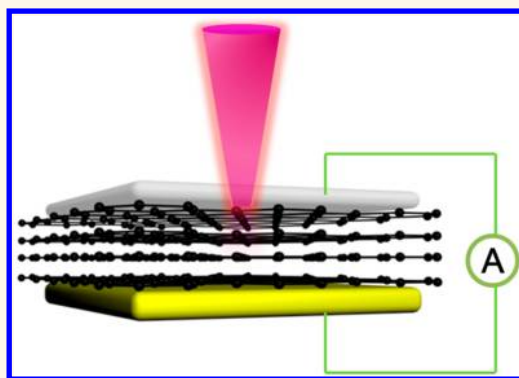


Photovoltaic Effect and Evidence of Carrier Multiplication in Graphene Vertical Homojunctions with Asymmetrical Metal Contacts

Jing-Jing Chen,^{†,‡} Qinsheng Wang,^{‡,‡} Jie Meng,[†] Xiaoxing Ke,[§] Gustaaf Van Tendeloo,[§] Ya-Qing Bie,[†] Junku Liu,^{‡,||} Kaihui Liu,^{†,⊥} Zhi-Min Liao,^{*,†,⊥} Dong Sun,^{*,†,⊥} and Dapeng Yu^{*,†,⊥}

[†]State Key Laboratory for Mesoscopic Physics, Department of Physics, Peking University, Beijing 100871, P. R. China, [‡]International Center for Quantum Materials, Peking University, Beijing 100871, P. R. China, [§]EMAT (Electron Microscopy for Materials Science), University of Antwerp, Groenenborgerlaan 171, B-2020 Antwerp, Belgium, ^{||}Qian Xuesen Laboratory of Space Technology, China Academy of Space Technology, Beijing 100094, P. R. China, and [⊥]Collaborative Innovation Center of Quantum Matter, Beijing 100084, P. R. China. ^{*}These authors contributed equally to this work.

ABSTRACT Graphene exhibits exciting potentials for high-speed wideband photodetection and high quantum efficiency solar energy harvest because of its broad spectral absorption, fast photoelectric response, and potential carrier multiplication. Although photocurrent can be generated near a metal–graphene interface in lateral devices, the photoactive area is usually limited to a tiny one-dimensional line-like interface region. Here, we report photoelectric devices based on vertical graphene two-dimensional homojunction, which is fabricated *via* vertically stacking four graphene monolayers with asymmetric metal contacts. The devices show excellent photovoltaic output with excitation wavelength ranging from visible light to mid-infrared. The wavelength dependence of the internal quantum efficiency gives direct evidence of the carrier multiplication effect in graphene. The simple fabrication process, easy scale-up, large photoresponsive active area, and broadband response of the vertical graphene device are very promising for practical applications in optoelectronics and photovoltaics.



KEYWORDS: graphene · photodetector · carrier multiplication · vertical homojunction · photovoltaics

Characterized by its gapless energy dispersion, graphene is known to generate electron–hole pairs over a broad light bandwidth from ultraviolet to the terahertz range.^{1–14} Photocurrent generation has been demonstrated in graphene near metallic contacts,^{6,7,15} at the lateral boundary between single-layer and bilayer regions,^{16,17} and at the edge of lateral p–n junctions.^{8,18,19} Nevertheless, the photocurrent away from the contacts or the boundaries is usually very weak and the intrinsically weak absorption of graphene limits the external quantum efficiency (EQE) to the range of merely ~0.1–1%. To overcome the limits of the small photoactive area and the weak absorption, heterostructures of graphene with two-dimensional (2D) semiconductors have been formed by stacking graphene layers

and transition metal dichalcogenides.^{20,21} Although the EQE is enhanced in such heterostructure, the spectral range of the photoelectric response is limited by the band gap of the 2D semiconductors. In this work, we demonstrate graphene–graphene vertical homojunctions that have a much larger photoactive area and maintain the broadband photo response meanwhile. Metal-stacked four layer graphene (SFLG)—metal vertical devices are fabricated *via* a layer-by-layer assembly method, where asymmetric metal contacts are employed to modulate the electronic states in the bottom and the top graphene layers. The as-built graphene–graphene junction is demonstrated as a photovoltaic cell that can be used as a self-powered photodetector without applying a source-drain bias.

* Address correspondence to
liaoqm@pku.edu.cn,
sundong@pku.edu.cn,
yudp@pku.edu.cn.

Received for review April 20, 2015
and accepted August 15, 2015.

Published online
10.1021/acs.nano.5b02356

© XXXX American Chemical Society

RESULTS AND DISCUSSION

A schematic metal–SFLG–metal device is shown in Figure 1a. The structure consists of four stacked graphene monolayers sandwiched between the top Ag electrode and the bottom Pt electrode fabricated on a Si/SiO₂ substrate. The fabricating procedure of the device is described in detail in Supporting Information Figure S1. A cross-sectional specimen from the as-built multilayer graphene photovoltaic cell is prepared and characterized by transmission electron microscopy (TEM), as shown in Figure 1b. It seems that the graphene layers are well attached to the top and bottom electrodes. When graphene is in contact with the metal, there will be electron transfer at the interface. Previous experiments suggest that the magnitude of the doping not only depends on the difference between the work functions of graphene Φ_G and metal Φ_M , but also on the wave function hybridization or chemical interaction which may contribute to the electronic doping of graphene.^{22,23} Theoretical calculations of metal on graphene predict the formation of an interfacial dipole layer, resulting in a potential step ($\Delta V = 0.9$ eV) to favor n-type doping in graphene *via* electron transfer from metal to graphene.²² Due to the existence of the interfacial dipole layer, it was demonstrated that a Pt film can produce either n-type or weak p-type doping of pristine graphene with Fermi level crossing the Dirac point, although Pt has a larger work function than graphene.²³ For our stacked graphene layers, the Fermi level initially locates below the Dirac point due to the

possible p-type doping induced in the graphene transfer procedure (Figure S2).²⁴ At the graphene/bottom Pt electrode interface, the electron transfer from Pt to graphene shifts up the Fermi level of the bottom graphene layer. In the case of the top electrode, Ag has a much smaller work function than Pt, and therefore, more electrons transfer from Ag to the top graphene layer, resulting in a much higher Fermi level of the top graphene layer. In a multilayer graphene system, it has been revealed that the screening effect is nonsaturated until the fourth layer.²⁵ The potential profile and the built-in electric field of the Ag–SFLG–Pt vertical device are illustrated in Figure 1c. Upon light absorption, electron–hole pairs can be separated by the built-in electric field within the graphene layers, resulting in a net current flowing from top Ag to bottom Pt through the inner vertical structure.

The configuration of the current–voltage (I – V) measurement and the optical image of a typical device are shown in Figure 1, panels d and e, respectively. The dashed box indicates the Ag–SFLG–Pt junction with an area of $\sim 10\ \mu\text{m} \times 10\ \mu\text{m}$, and the green dot indicates the focused laser. The vertical device shows linear I – V curves and a photovoltaic effect under illumination (Figure 1f). The fill factor, which is the ratio of the actual maximum output power to the product of the open circuit voltage and short circuit current, is calculated to be 0.25. The efficiency, which is measured as the ratio of useful output to total input, is calculated to be 1.15×10^{-8} . One of the reasons for such a low

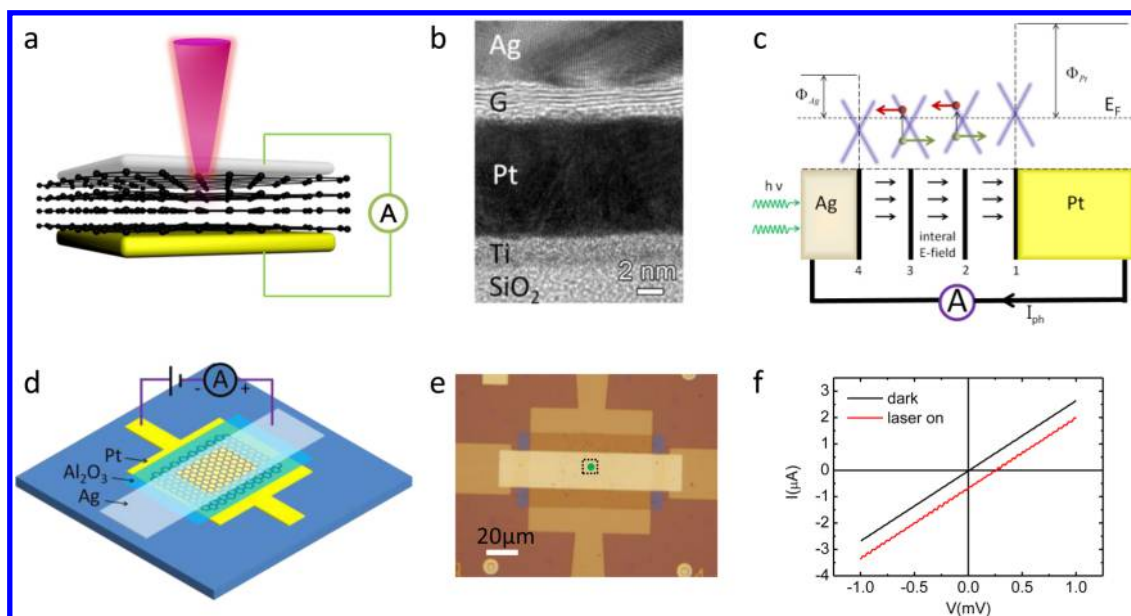


Figure 1. Structure and mechanism of the vertical Ag-stacked graphene layers-Pt photovoltaic cell. (a) Schematic of the vertical device. (b) Cross-sectional HRTEM image of the Ag–SFLG–Pt junction. (c) Schematic band diagram of the vertical structure. Red and green spots represent photoexcited electrons and holes, respectively, and the corresponding arrows indicate the transport directions. Φ_{Ag} and Φ_{Pt} are the work function of Ag and Pt, respectively. I_{ph} is the photocurrent. The four graphene layers are denoted by the numbers “1, 2, 3, 4”, and the black arrows present the built-in electric field. (d) Sketch of the measurement configuration of a vertical Ag–SFLG–Pt device. (e) Optical image of a typical device. The dashed box denotes the Ag–SFLG–Pt junction with an area of $\sim 10\ \mu\text{m} \times 10\ \mu\text{m}$, and the green dot indicates the focused laser spot. (f) I – V characteristics recorded in the dark and under laser irradiation.

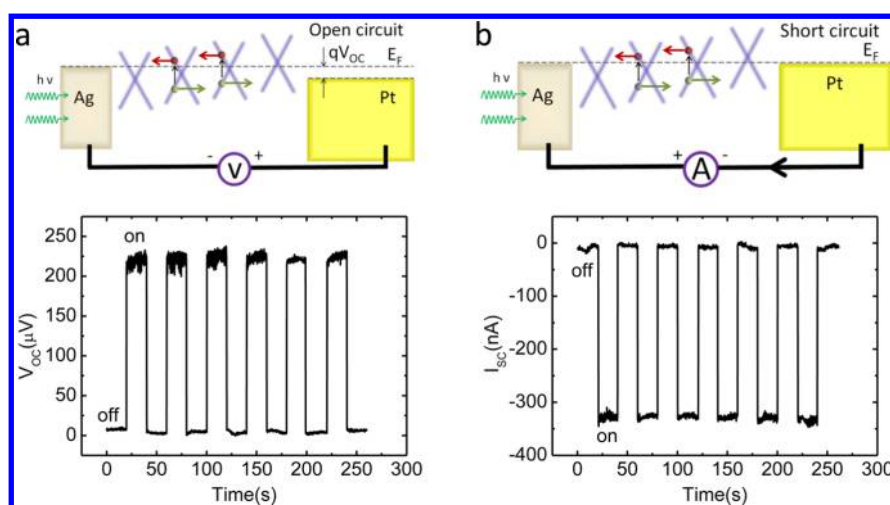


Figure 2. Performances of vertical Ag–SFLG–Pt device. The photoelectrical properties were measured under laser irradiation with 514 nm wavelength. (a) The mechanisms of the photogenerated open-circuit voltage (V_{OC} , upper panel) and the V_{OC} outputs under on–off light modulation (lower panel). (b) The mechanisms of the photogenerated short-circuit current (I_{SC} , upper panel) and the I_{SC} outputs under on–off light modulation (lower panel).

efficiency is the top Ag attenuates most light. The open-circuit voltage and short-circuit current switch between on/off states as switching on/off the laser illumination, and polarities of the measured voltage and current are well consistent with the mechanisms of the electron–hole pair separation in the built-in electric field between the graphene layers (Figure 2). The polarities of the photo generated voltage and current reverse when exchanging the electrical connections of the device (Figure S3), indicating that the measured signals are from the device. The response time cannot be directly retrieved from our measurement (Figure S4), and we estimate the intrinsic response time of the vertical graphene detector is below nanosecond according to previous study of graphene based photodetector.^{6,8}

To separate the photocurrent contributions from different interfaces, we fabricated devices with only a graphene/bottom Pt electrode interface, a top Pt electrode/graphene interface, and Pt/graphene layers/Pt interfaces, respectively (Figure S5). The I – V characteristics of the three devices are shown in (Figure S6), and the minor differences of their resistances will not lead to the significant differences of the open-circuit voltages. For the device with graphene/bottom Pt interface (Figures 3a–c), the photovoltage shows a negative polarity, which is opposite to the device with a top Pt/graphene interface (Figures 3d–f). Although the two devices have an equivalent magnitude of photovoltage $\sim 100 \mu V$, the top Pt/SFLG device has a higher internal quantum efficiency because the top Pt allows only 3.84% light transmission (Figure S7). It suggests that the top Pt–graphene interface produces a sharper potential profile than the bottom graphene–Pt interface. The top Pt electrode was deposited directly on the graphene surface by e-beam thermal evaporation under high vacuum, resulting in a better contact than that of bottom graphene/Pt

interface formed by a transfer technique. Therefore, a symmetrical electrode configuration with Pt–SFLG–Pt structure also has an asymmetric electronic band potential which simplifies the fabrication process of such device.

Twelve Pt–SFLG–Pt devices were fabricated to study their photoelectric properties. The cross-sectional TEM image of the Pt–SFLG–Pt junction is shown in Figure 4a. No clear contaminations can be found, which may be introduced during the graphene transfer process. The measurement configuration is shown in Figure 4b. The mechanism of the photogenerated open-circuit voltage is shown in Figure 4c. All Pt–SFLG–Pt devices show a positive photovoltage, indicating that the photovoltage generation is dominated by the graphene doping from the top Pt electrode, although the graphene/bottom Pt interface tends to decrease the potential slope produced by the top Pt/graphene interface. Surprisingly, as shown in Figure 4d, the vertical Pt–SFLG–Pt device (with 300 μV photovoltage) performed better than the top Pt/SFLG device (with 100 μV photovoltage, Figure 3f) under the same excitation conditions. This implies that the vertical Pt–SFLG–Pt structure makes the carrier collection much more efficient than the top Pt/SFLG structure. The photoexcited electron–hole pairs would typically decay on a time scale of tens of picoseconds,⁹ and the carrier-diffusion length is typically ~ 15 –70 nm.²⁶ For our vertical structure, the distance between the electrodes is several nanometers, which is shorter than the carrier-diffusion length, resulting in a more efficient transit of the photoexcited electron–hole pairs toward opposite electrodes.

Furthermore, the metal–SFLG–metal device has a broadband photoelectric response due to the zero bandgap of graphene. Figure 4e shows that the device still works well in the mid-infrared region with a

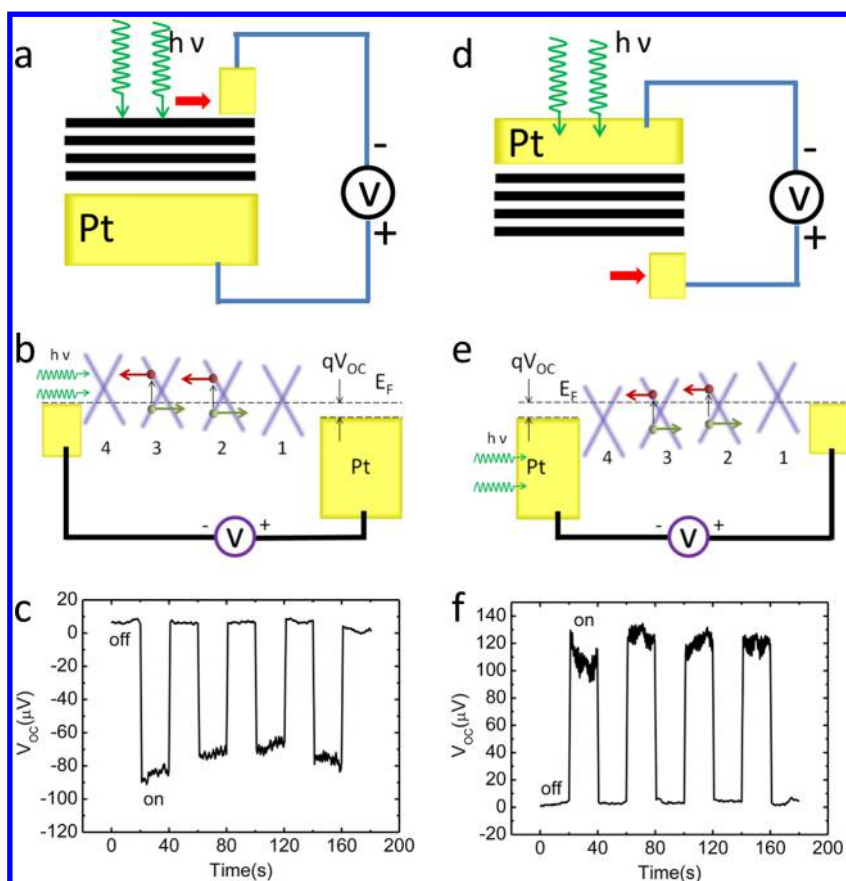


Figure 3. The role of interface on the photovoltage generation. Structures, mechanisms, and photovoltages of two devices with graphene/bottom Pt interface, top Pt/graphene interface. (a–c) Structure, mechanism, and photovoltage of the device with graphene/bottom Pt interface, respectively. (d–f) Structure, mechanism, and photovoltage of the device with top Pt/graphene interface, respectively. The red arrows in (a) and (d) indicate that carriers away from the electrode must diffuse laterally to the electrode to be collected.

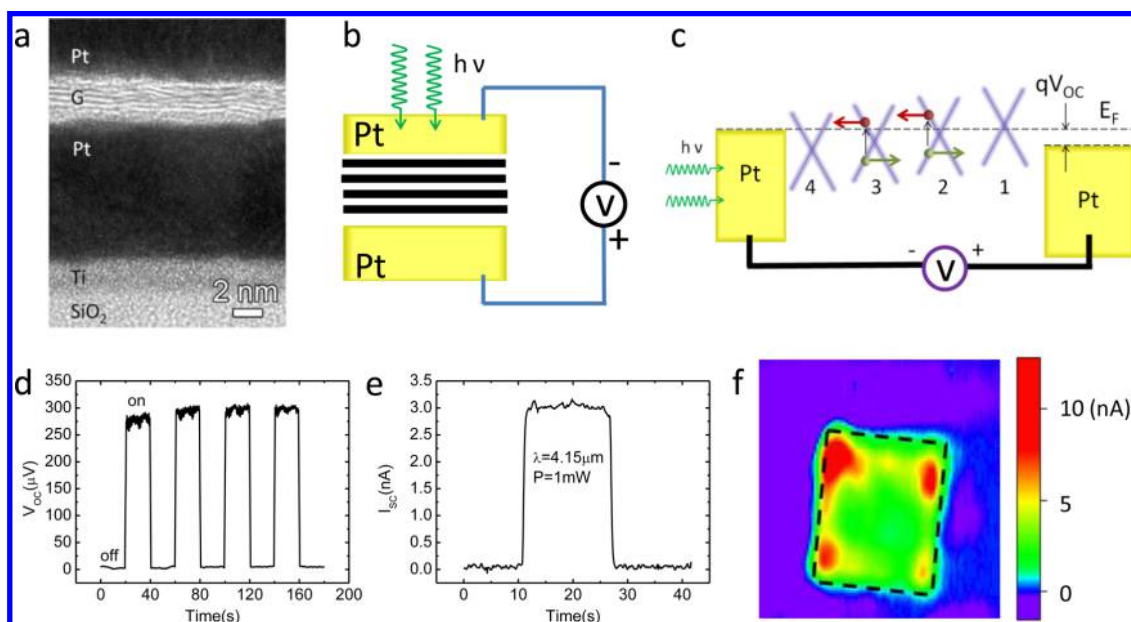


Figure 4. Vertical Pt-four-stacked-graphene-Pt device. (a) A cross-sectional TEM image of the Pt–SFLG–Pt junction. (b–d) Measurement configuration, mechanism, and photovoltage with excitation by a 514 nm laser, respectively. (e) Photocurrent generation excited by a 4.15 μm laser. (f) Scanning photocurrent mapping of the device under a 800 nm laser excitation.

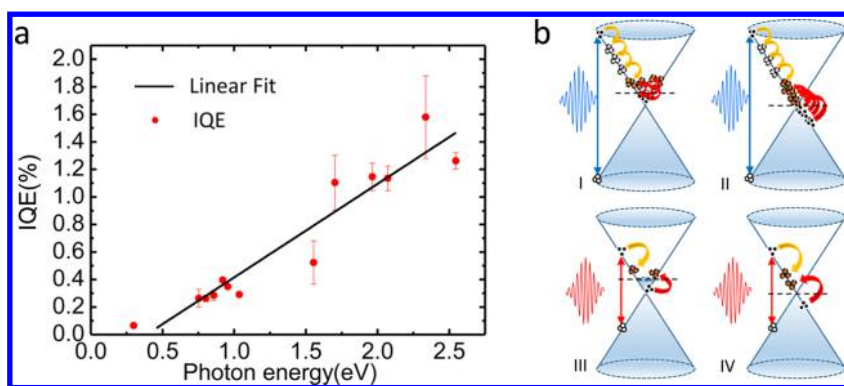


Figure 5. Carrier multiplication effect in the Pt–SFLG–Pt device. (a) Photon energy dependence of the internal quantum efficiency from 488 to 4150 nm; the excitation photon fluence on the device is kept around $10^{13}/\text{cm}^2$. The measured photon energy dependent IQE can be fit linearly. (b) Illustration of the carrier multiplication process under different excitation photon energy in doped (I, III) and undoped graphene layers (II, IV). Yellow arrows show the cascade relaxation steps of photoexcited carriers. Red arrows show intraband impact excitation in doped layers and interband impact excitation in undoped layers. Higher photon energy excitation (I, II) can induce more steps of impact excitation cascade and thus result in larger internal quantum efficiency.

wavelength of $4.15\ \mu\text{m}$. The photoelectric response from visible light to mid-infrared ($4.15\ \mu\text{m}$) is demonstrated and shown in Figure S8. It must be noted that the device is expected to work beyond this wavelength range, but measurements at other wavelengths were limited by the available light source. Unlike the lateral graphene–metal junctions or graphene p–n junctions that have a rather small photoactive area near the junction, this vertical device can generate a photocurrent throughout the entire area of the metal–SFLG–metal junction, as shown in the scanning photocurrent mapping (Figure 4f). The enhancement of the photocurrent at the corners and edge of Figure 4f is due to thinning of the Pt contact at the steps between graphene and Al_2O_3 during the Pt deposition process (Figure S9) and the enhancement is universal in all devices that are measured. This unique advantage of graphene vertical homojunctions allows us to compare the internal quantum efficiency (IQE) of different photon excitation energy. The wavelength dependent measurement of IQE is performed on a $10\ \mu\text{m} \times 10\ \mu\text{m}$ Pt–SFLG–Pt device. This active area is slightly larger than the spot size of the laser excitation used in this measurement. The IQE (η) is defined as the number of photocarriers collected in the external circuits to the number of photons actually absorbed in graphene, that is, $\eta = [I_{\text{ph}}/e][h\nu/\alpha P_{\text{in}}]$, where I_{ph} is the photocurrent, e is the electron charge, h is Planck's constant, ν is the frequency of light, α is the ratio of the absorbed light by graphene to the total incident light, and P_{in} is the total incident optical power. Taking into account the light transmission of the top Pt electrode, the incident power arriving at graphene is attenuated and has wavelength dependence as shown in Figure S7. The wavelength dependent absorption rate of the graphene is taken from the measurements by Mak *et al.*,^{27–29} and thus, the absorption of 4-layer graphene to different photon energy can be deducted through standard transfer

matrix calculation described in the Supporting Information (Figures S10 and S11). We can see from Figure 5a that the IQE increases linearly with the excitation photon energy, giving one of the most notable signatures of the carrier multiplication process in graphene,^{10,30} which plays the key role in enhancing the photon harvest efficiency in the photodetector and solar cell. The carrier multiplication process is schematically shown in Figure 5b. During the relaxation of photon excited hot carriers, instead of losing their energy to the lattice (phonons), the carriers prefer to transfer their energy to secondary electrons and create additional electron–hole pairs through interband transition in the undoped layers (II, IV of Figure 5b, referred as conventional carrier multiplication). Additionally, hot carriers can be created in the doped layers through intraband transition (I, III of Figure 5b, referred as “hot carrier multiplication” following the reference), leading to the efficient photocurrent generation through photo thermoelectric effect in graphene.^{8,10,16,18} Both processes are highly efficient and can cascade many times due to graphene's zero bandgap and highly efficient carrier–carrier scattering in linear dispersion band structure.^{31–33} In this scenario, the generation of multiple electron–hole pairs (conventional carrier multiplication) or hot carriers (hot carrier multiplication) from the absorption of a single photon is possible in graphene. As both carrier multiplication and hot carrier multiplication have IQEs that are linearly dependent on excitation photon energy,^{10,30} the wavelength dependent IQE measurement in this work cannot distinguish the dominant mechanism, whether it is built-in electric field or photothermoelectric effect, in the response of the device. The sign of the thermoelectric current in a p⁺–p junction can exhibit the same or opposite sign as that of a p–n sample.¹⁸ As shown in Figure 1c, p⁺–p, p–n, and n–n⁺ junctions may coexist in our vertical structure. Thermoelectric current generated by the three junctions may weaken or enhance

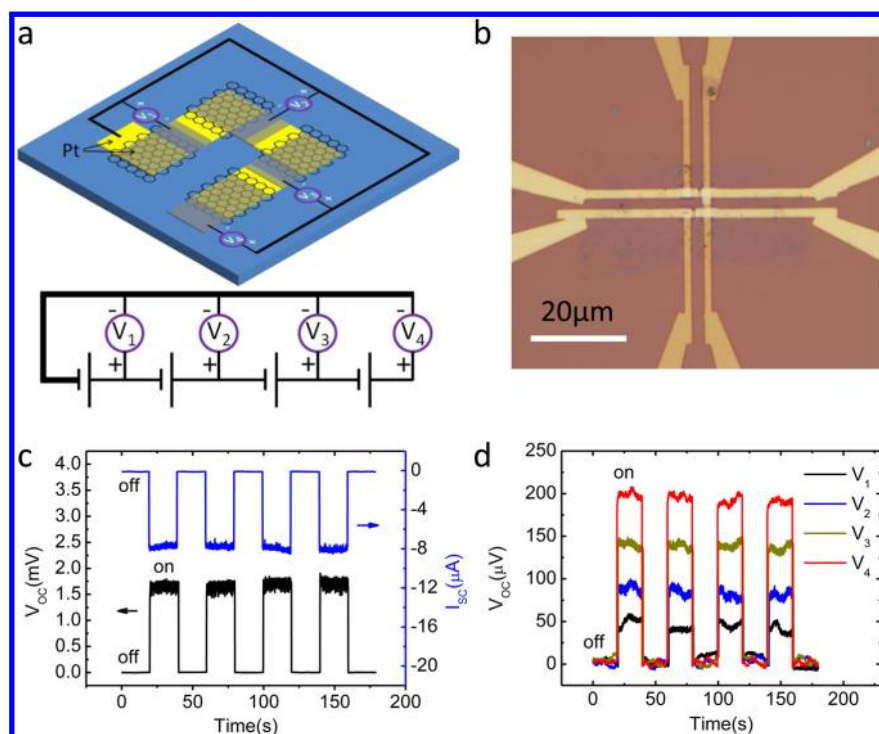


Figure 6. Four individual cells connected in series. (a) Schematic of a general device consisting of four individual Pt–SFLG–Pt cells. V_1 , V_2 , V_3 , and V_4 measure the tandem cells with one, two, three, and four individual cells connected in series, respectively. (b) Optical image of a typical device composed by four Pt–SFLG–Pt cells. (c) Photoresponse of a single Pt–SFLG–Pt cell under on–off light modulation of a 514 nm laser with an excitation power of ~ 3.79 mW. (d) Photovoltage for the tandem cells with one (V_1), two (V_2), three (V_3), and four (V_4) individual cells connected in series, as the laser spot is expanded to cover all four individual cells with reduced power density.

each other, depending on the carrier densities. In contrast, photocurrent generated by the built-in electric field must enhance each other. The polarity of the photocurrent generated by the built-in electric field is inconsistent with the result. At least, the built-in electric field effect makes positive contribution to the total photocurrent. To distinguish the photothermoelectric effect and built-in electric field effect, further smoking gun experiment is desired on this vertical device, such as temperature dependence and autocorrelation measurement of the photocurrent.⁸ Here, we emphasize that although carrier multiplication and hot carrier multiplication have been theoretically proposed^{31,33} and indirectly measured by pump probe experiments,^{10,11,32,34} time-resolved angle-resolved photoemission spectroscopy,³⁵ our experiment provides direct evidence of this important optoelectronic effect in a real graphene based functional detector, although the IQE is still relatively low in this measurement, possibly due to the gentle slope of the band profile between graphene layers. For future work, a larger built-in electric field throughout the entire vertical device could be designed by applying a proper electrode which can heavily dope the graphene. Besides, the resistance of the thin Pt electrodes (30 nm with 386 Ω) contributes to the majority of the total resistance of the Pt–SFLG–Pt device (450 Ω), which accounts for the 6-fold decrease in photocurrent. A transparent and conductive electrode

that favors the doping in graphene and minimizes the series resistance of the electrode is the best choice for the top electrode.³⁶ Finally, a significant improvement could be achieved by enhancing the light absorption of graphene. As a comparative example, a metal-stacked two layer graphene–metal device (Figure S12) was also fabricated, generating about half the amount of the photocurrent compared to the SFLG based device. We attribute this improvement to the enhancement of the light absorption in four-stacked-graphene layers.

The graphene vertical structure based photocell is scalable, demonstrating its potential for solar energy harvest. For a conceptual demonstration, we fabricated a structure composed of four individual cells connected in series, as shown in Figure 6a,b. Fabrication details are shown in Figure S13. The performance of the four individual cells was characterized by a 514 nm laser with an excitation power of ~ 3.79 mW. Figure 6c shows the open-circuit voltage and the short-circuit current when switching the illumination for one Pt–SFLG–Pt cell. The photovoltage and photocurrent are 1.5 mV and 8 μ A, respectively. The responsivity (defined as I_{ph}/P_{in}) was calculated to be 2.1 mA/W. The laser spot was then enlarged to cover the complete area of all four cells, resulting in a decrease in the power density from 134 to 5.36 μ W/ μ m². Figure 6d presents photovoltages for the tandem cells with one to four individual cells connected in series. The photovoltage

outputs are 45, 85, 140, and 197 μV for the single cell, double-cell module, triple cell module, and quadruple cell module, respectively, which are well consistent with the series circuit voltage output.

CONCLUSIONS

In summary, we have demonstrated that vertical metal–SFLG–metal can be constructed to generate photocurrent over a broad light bandwidth with a large scalable junction area. Metal electrodes are designed to modulate asymmetrically the graphene Fermi

level at the top electrode/graphene and the bottom electrode/graphene interfaces. The device achieves responsivity up to 2.1 mA/W and shows evidence of the carrier multiplication effect. The simple fabrication process, large photoresponsive active area and broadband photoresponse hold great promise for practical applications in photoelectronic devices. Further optimizations of the number of graphene layers and improvement of the top electrodes could open up new prospects of high-performance optoelectronic devices.

MATERIALS AND METHODS

Fabrication of Stacked Four-Layer Graphene. A PMMA thin layer was spin-coated onto a monolayer graphene surface grown on a copper foil. The Cu foil was then dissolved by a FeCl_3 saturated solution for 30 min. The graphene/PMMA film was washed three times in 60 $^\circ\text{C}$ deionized water. Another monolayer graphene on copper foil was used to fish out the graphene/PMMA film from deionized water. The face-to-face adhesion of the clean graphene surfaces allows no PMMA between the graphene layers. The two-layer graphene/PMMA film was then patterned into microstamps via electron beam lithography (EBL) and O_2 plasma etching. After the Cu foil was dissolved and the two-layer graphene/PMMA film was rinsed, the two-layer graphene/PMMA microstamps can be transferred and printed onto the bottom electrode. The fabrication process and the detailed structure are shown in Figure S1. First, the bottom electrode was fabricated using EBL, followed by metal deposition of Ti/Pt (5/15 nm) and a lift-off. Then, the two-layer graphene/PMMA stack was transferred onto the bottom electrode;³⁷ subsequently, the PMMA was dissolved by acetone (Figure S1b). Another two-layer graphene/PMMA was transferred and stacked to form the stacked four layer graphene. Finally, after removing the PMMA by acetone, an insulating Al_2O_3 layer (25 nm) with a window of $10\ \mu\text{m} \times 10\ \mu\text{m}$ in the center of the graphene was fabricated via EBL and film deposition, as shown in Figure S1c. The last step was to fabricate the top electrode by another round of EBL and metal deposition of Pt (30 nm) via electron-beam evaporation.

Cross-Sectional Sample Preparation and TEM Characterization. After depositing a protective layer of amorphous carbon and subsequently Pt on the device surface, a thin cross section lamella was prepared by Focused Ion Beam (FIB) using a FEI-Helios Nano-LabDualBeam system. Special care is taken when milling the structure in order to protect the graphene layer. High-resolution TEM characterization was performed on a FEI Tecnai G2 microscope operated at 200 kV.

Photocurrent Measurement. All measurements were performed in ambient conditions at room temperature. Except for the wavelength dependent response and the photocurrent mapping, all electrical measurements were performed by Agilent B2912, and the optical excitations were carried out by a 514 nm laser guided by a Renishaw Raman optical system. For wavelength-dependent IQE measurement, a series of bandpass filters are used to select the desired wavelength from an ultrafast fiber laser (Fianium: WhiteLase-Micro) which generates a supercontinuum white light with wavelength from 450 to 2200 nm. The repetition rate of the Fianium is 20 MHz and the pulse width is 6 ps. The laser was focused on the device active area by a $20\times$ (Olympus LMPlanFLN $20\times/0.40$) objective in the visible wavelength or a $40\times$ reflective objective (thorlabs LMM-40 \times -UVV, 0.5NA) in the near-IR wavelength. The spot sizes are all within the $10\text{-}\mu\text{m}$ device active area and the photon fluence is kept around $10^{13}/\text{cm}^2$. For the 4- μm measurement, 250 kHz Coherent RegA pumped infrared optical parametric amplifier (OPA), followed by a differential frequency generator (DFG), is used to generate mid-IR pulse with a pulse width of 300 fs. A ZnSe Focusing

objective (0.2 NA) in the mid-IR range is used to focus the mid-IR. The laser was modulated with a mechanic chopper with a frequency around 1.5 kHz and the generated photocurrent was converted to voltage using a current preamplifier (DL instruments 1211); then, the voltage was read out by a Lock in amplifier (SR 830) referred to the mechanical chopper.

Conflict of Interest: The authors declare no competing financial interest.

Acknowledgment. This work was supported by MOST (Nos. 2013CB934600, 2013CB932602, 2012CB921300 and 2014CB920900), NSFC (Nos. 11274014, 11234001, 11274015), the Program for New Century Excellent Talents in University of China (No. NCET-12-0002) and the Recruitment Program of Global Experts. XK and GVT acknowledge support of the ERC grant COUNTATOMS.

Supporting Information Available: The Supporting Information is available free of charge on the ACS Publications website at DOI: 10.1021/acs.nano.5b02356.

Fabrication of Ag–SFLG–Pt device, doping level of stacked graphene monolayers, devices with a graphene/bottom Pt electrode interface, top Pt electrode/graphene interface, top Pt electrode/graphene/bottom Pt electrode interfaces, wavelength-dependent transmission of the 30 nm-thick Pt film, wavelength-dependent photoresponse of the Pt–SFLG–Pt device, performances of the Ag-stacked two layer graphene–Pt and Ag-stacked four layer graphene–Pt devices, fabrication process of a general device consisting of four individual Pt–SFLG–Pt photocells (PDF)

REFERENCES AND NOTES

- Avouris, P.; Xia, F. Graphene Applications in Electronics and Photonics. *MRS Bull.* **2012**, *37*, 1225–1234.
- Liu, C.-H.; Chang, Y.-C.; Norris, T. B.; Zhong, Z. Graphene Photodetectors with Ultra-Broadband and High Responsivity at Room Temperature. *Nat. Nanotechnol.* **2014**, *9*, 273–278.
- Ju, L.; Geng, B.; Horng, J.; Girit, C.; Martin, M.; Hao, Z.; Bechtel, H. A.; Liang, X.; Zettl, A.; Shen, Y. R.; et al. Graphene Plasmonics for Tunable Terahertz Metamaterials. *Nat. Nanotechnol.* **2011**, *6*, 630–634.
- Fuhrer, M. S.; Lau, C. N.; MacDonald, A. H. Graphene: Materially Better Carbon. *MRS Bull.* **2010**, *35*, 289–295.
- Liu, M.; Yin, X.; Ulin-Avila, E.; Geng, B.; Zentgraf, T.; Ju, L.; Wang, F.; Zhang, X. A Graphene-Based Broadband Optical Modulator. *Nature* **2011**, *474*, 64–67.
- Xia, F.; Mueller, T.; Lin, Y.-m.; Valdes-Garcia, A.; Avouris, P. Ultrafast Graphene Photodetector. *Nat. Nanotechnol.* **2009**, *4*, 839–843.
- Mueller, T.; Xia, F.; Avouris, P. Graphene Photodetectors for High-Speed Optical Communications. *Nat. Photonics* **2010**, *4*, 297–301.
- Sun, D.; Aivazian, G.; Jones, A. M.; Ross, J. S.; Yao, W.; Cobden, D.; Xu, X. Ultrafast Hot-Carrier-Dominated Photocurrent in Graphene. *Nat. Nanotechnol.* **2012**, *7*, 114–118.

9. Sun, D.; Wu, Z.-K.; Divin, C.; Li, X.; Berger, C.; de Heer, W. A.; First, P. N.; Norris, T. B. Ultrafast Relaxation of Excited Dirac Fermions in Epitaxial Graphene Using Optical Differential Transmission Spectroscopy. *Phys. Rev. Lett.* **2008**, *101*, 157402.
10. Tielrooij, K. J.; Song, J. C. W.; Jensen, S. A.; Centeno, A.; Pesquera, A.; Zurutuza Elorza, A.; Bonn, M.; Levitov, L. S.; Koppens, F. H. L. Photoexcitation Cascade and Multiple Hot-Carrier Generation in Graphene. *Nat. Phys.* **2013**, *9*, 248–252.
11. Brida, D.; Tomadin, A.; Manzoni, C.; Kim, Y. J.; Lombardo, A.; Milana, S.; Nair, R. R.; Novoselov, K. S.; Ferrari, A. C.; Cerullo, G.; et al. Ultrafast Collinear Scattering and Carrier Multiplication in Graphene. *Nat. Commun.* **2013**, *4*, 1987.
12. Novoselov, K. S.; Geim, A. K.; Morozov, S. V.; Jiang, D.; Katsnelson, M. I.; Grigorieva, I. V.; Dubonos, S. V.; Firsov, A. A. Two-Dimensional Gas of Massless Dirac Fermions in Graphene. *Nature* **2005**, *438*, 197–200.
13. Zhang, Y.; Tan, Y.-W.; Stormer, H. L.; Kim, P. Experimental Observation of the Quantum Hall Effect and Berry's Phase in Graphene. *Nature* **2005**, *438*, 201–204.
14. Pospischil, A.; Humer, M.; Furchi, M. M.; Bachmann, D.; Guider, R.; Fromherz, T.; Mueller, T. CMOS-Compatible Graphene Photodetector Covering All Optical Communication Bands. *Nat. Photonics* **2013**, *7*, 892–896.
15. Park, J.; Ahn, Y. H.; Ruiz-Vargas, C. Imaging of Photocurrent Generation and Collection in Single-Layer Graphene. *Nano Lett.* **2009**, *9*, 1742–1746.
16. Xu, X.; Gabor, N. M.; Alden, J. S.; van der Zande, A. M.; McEuen, P. L. Photo-Thermoelectric Effect at a Graphene Interface Junction. *Nano Lett.* **2010**, *10*, 562–566.
17. Wang, F.; Zhang, Y.; Tian, C.; Girit, C.; Zettl, A.; Crommie, M.; Shen, Y. R. Gate-Variable Optical Transitions in Graphene. *Science* **2008**, *320*, 206–209.
18. Gabor, N. M.; Song, J. C. W.; Ma, Q.; Nair, N. L.; Taychatanapat, T.; Watanabe, K.; Taniguchi, T.; Levitov, L. S.; Jarillo-Herrero, P. Hot Carrier-Assisted Intrinsic Photoresponse in Graphene. *Science* **2011**, *334*, 648–652.
19. Lemme, M. C.; Koppens, F. H. L.; Falk, A. L.; Rudner, M. S.; Park, H.; Levitov, L. S.; Marcus, C. M. Gate-Activated Photoresponse in a Graphene p–n Junction. *Nano Lett.* **2011**, *11*, 4134–4137.
20. Yu, W. J.; Liu, Y.; Zhou, H.; Yin, A.; Li, Z.; Huang, Y.; Duan, X. Highly Efficient Gate-Tunable Photocurrent Generation in Vertical Heterostructures of Layered Materials. *Nat. Nanotechnol.* **2013**, *8*, 952–958.
21. Britnell, L.; Ribeiro, R. M.; Eckmann, A.; Jalil, R.; Belle, B. D.; Mishchenko, A.; Kim, Y.-J.; Gorbachev, R. V.; Georgiou, T.; Morozov, S. V.; et al. Strong Light-Matter Interactions in Heterostructures of Atomically Thin Films. *Science* **2013**, *340*, 1311–1314.
22. Giovannetti, G.; Khomyakov, P. A.; Brocks, G.; Karpan, V. M.; van den Brink, J.; Kelly, P. J. Doping Graphene with Metal Contacts. *Phys. Rev. Lett.* **2008**, *101* (101), 026803.
23. Pi, K.; McCreary, K. M.; Bao, W.; Han, W.; Chiang, Y. F.; Li, Y.; Tsai, S. W.; Lau, C. N.; Kawakami, R. K. Electronic Doping and Scattering by Transition Metals on Graphene. *Phys. Rev. B: Condens. Matter Mater. Phys.* **2009**, *80*, 075406.
24. Chen, J.-J.; Meng, J.; Zhou, Y.-B.; Wu, H.-C.; Bie, Y.-Q.; Liao, Z.-M.; Yu, D.-P. Layer-by-Layer Assembly of Vertically Conducting Graphene Devices. *Nat. Commun.* **2013**, *4*, 1921.
25. Sun, D.; Divin, C.; Berger, C.; de Heer, W. A.; First, P. N.; Norris, T. B. Spectroscopic Measurement of Interlayer Screening in Multilayer Epitaxial Graphene. *Phys. Rev. Lett.* **2010**, *104*, 136802.
26. Mueller, T.; Xia, F.; Freitag, M.; Tsang, J.; Avouris, P. Role of Contacts in Graphene Transistors: A Scanning Photocurrent Study. *Phys. Rev. B: Condens. Matter Mater. Phys.* **2009**, *79*, 245430.
27. Mak, K. F.; Matthew, Y. S.; Wu, Y.; Lui, C. H.; Misewich, J. A.; Heinz, T. F. Measurement of the Optical Conductivity of Graphene. *Phys. Rev. Lett.* **2008**, *101*, 196405.
28. Mak, K. F.; Shan, J.; Heinz, T. F. Seeing Many-Body Effects in Single- and Few-Layer Graphene: Observation of Two-Dimensional Saddle-Point Excitons. *Phys. Rev. Lett.* **2011**, *106*, 046401.
29. Mak, K. F.; Ju, L.; Wang, F.; Heinz, T. F. Optical Spectroscopy of Graphene: from the Far Infrared to the Ultraviolet. *Solid State Commun.* **2012**, *152*, 1341.
30. Winzer, T.; Malic, E. Impact of Auger Processes on Carrier Dynamics in Graphene. *Phys. Rev. B: Condens. Matter Mater. Phys.* **2012**, *85*, 241404.
31. Basko, D. M. Effect of Anisotropic Band Curvature on Carrier Multiplication in Graphene. *Phys. Rev. B: Condens. Matter Mater. Phys.* **2013**, *87*, 165437.
32. Plotzing, T.; Winzer, T.; Malic, E.; Neumaier, D.; Knorr, A.; Kurtz, H. Experimental Verification of Carrier Multiplication in Graphene. *Nano Lett.* **2014**, *14*, 5371–5375.
33. Winzer, T.; Knorr, A.; Malic, E. Carrier Multiplication in Graphene. *Nano Lett.* **2010**, *10*, 4839–4843.
34. Tielrooij, K. J.; Piakowski, L.; Massicotte, M.; Woessner, A.; Ma, Q.; Lee, Y.; Myhro, S.; Lau, C. N.; Jarillo-Herrero, P.; van Hulst, N. F.; et al. Generation of Photovoltage in Graphene on a Femtosecond Timescale through Efficient Carrier Heating. *Nat. Nanotechnol.* **2015**, *10*, 437–443.
35. Gierz, I.; Petersen, J. C.; Mitran, M.; Cacho, C.; Turcu, I. C. E.; Springate, E.; Stohr, A.; Kohler, A.; Starke, U.; Cavalleri, A. Snapshots of Non-Equilibrium Dirac Carrier Distributions in Graphene. *Nat. Mater.* **2013**, *12*, 1119–1124.
36. Wu, H.; Kong, D.; Ruan, Z.; Hsu, P.-C.; Wang, S.; Yu, Z.; Carney, T. J.; Hu, L.; Fan, S.; Cui, Y. A Transparent Electrode Based on a Metal Nanotrough Network. *Nat. Nanotechnol.* **2013**, *8*, 421–425.
37. Bie, Y.-Q.; Zhou, Y.-B.; Liao, Z.-M.; Yan, K.; Liu, S.; Zhao, Q.; Kumar, S.; Wu, H.-C.; Duesberg, G. S.; Cross, G. L. W.; et al. Site-Specific Transfer-Printing of Individual Graphene Microscale Patterns to Arbitrary Surfaces. *Adv. Mater.* **2011**, *23*, 3938–3943.